Medical Image Analysis xxx (2013) xxx–xxx

Contents lists available at SciVerse ScienceDirect

Medical Image Analysis

journal homepage: www.elsevier.com/locate/media

In vivo human cardiac fibre architecture estimation using shape-based diffusion tensor processing

Nicolas Toussaint [a,b], Christian T. Stoeck [c], Tobias Schaeffter [a], Sebastian Kozerke [c,a], Maxime Sermesant [b,*], Philip G. Batchelor [a]

[a] *King's College London, Division of Imaging Sciences and Biomedical Engineering, The Rayne Institute, St. Thomas' Hospital, London SE1 7EH, United Kingdom*
[b] *Inria, Asclepios Research Project, 2004 route des Lucioles, 06902 Sophia-Antipolis, France*
[c] *University and ETH Zürich, Institute for Biomedical Engineering, Gloriastrasse 35, 8092 Zürich, Switzerland*

ARTICLE INFO

Article history:
Received 16 February 2012
Received in revised form 27 November 2012
Accepted 16 February 2013
Available online xxxx

Keywords:
Diffusion tensor imaging
Cardiac
In vivo
Elevation angle
Prolate spheroidal coordinates

ABSTRACT

In vivo imaging of cardiac 3D fibre architecture is still a practical and methodological challenge. However it potentially provides important clinical insights, for example leading to a better understanding of the pathophysiology and the follow up of ventricular remodelling after therapy. Recently, the acquisition of 2D multi-slice Diffusion Tensor Images (DTI) of the *in vivo* human heart has become feasible, yielding a limited number of slices with relatively poor signal-to-noise ratios. In this article, we present a method to analyse the fibre architecture of the left ventricle (LV) using shape-based transformation into a normalised Prolate Spheroidal coordinate frame. Secondly, a dense approximation scheme of the complete 3D cardiac fibre architecture of the LV from a limited number of DTI slices is proposed and validated using *ex vivo* data. Those two methods are applied *in vivo* to a group of healthy volunteers, on which 2D DTI slices of the LV were acquired using a free-breathing motion compensated protocol. Results demonstrate the advantages of using curvilinear coordinates both for the anaylsis and the interpolation of cardiac DTI information. Resulting *in vivo* fibre architecture was found to agree with data from previous studies on *ex vivo* hearts.

1. Introduction

Cardiac fibre architecture is fundamental to the cardiac function, as it influences the muscle's electrophysiological and mechanical properties. For instance, the electrical propagation is three times faster along the fibre direction than along its orthogonal plane (Kanai and Salama, 1995). Moreover, cardiac contraction is mainly explained by the arrangement of fibres (Bovendeerd et al., 1992; Anderson et al., 2008). For these reasons its study can have an important impact on clinical decisions, as several cardiac pathologies – such as myocardial infarction, cardiomyopathy, hypertension or valvular heart diseases – involve a rearrangement of myocardial fibres (Sutton and Sharpe, 2000; Helm et al., 2006).

Diffusion Tensor MRI (DTI) can image non-invasively the fibre orientation distribution of the myocardium (Hsu et al., 1998; Basser et al., 2000; Scollan et al., 2000; Holmes et al., 2000). Moreover, the intrinsic laminar sheet structure can also be revealed by taking into account the full information given by the tensors (Helm et al., 2005; Peyrat et al., 2006; Lombaert et al., 2011b). However, translating these techniques to the *in vivo* setting is extremely challenging (Sosnovik et al., 2009). Indeed, the displacements due to diffusion measured in DTI are three orders of magnitude smaller than the bulk motion of the heart, resulting in inaccurate diffusion signal. To tackle this problem, Reese et al. (1995) introduced a method based on stimulated echo acquisition (STE) where the diffusion signal is integrated over the entire heart beat. Later, improved by Tseng et al. (1999), this approach has been applied in 2D and proven useful for the depiction of clinically relevant information in several scenarios (Dou et al., 2003; Wu et al., 2009; Nielles-Vallespin et al., 2011; Sosnovik et al., 2009). Alternatively, Gamper et al. (2007) proposed a method that uses a standard spin echo (SE) technique in order to improve the Signal to Noise Ratio (SNR) efficiency. By means of bipolar gradient lobes, this technique only remains sensitive to acceleration and higher order motion, and enables the acquisition of 2D diffusion images. These techniques remain challenging to apply in practice. Due to time constraints, the amount of slices acquired is very limited and the SNR performances can be poor. It is therefore of interest to investigate and adapt the analysis and post-processing procedures to such specific situations.

---

* Corresponding author at: Inria, Asclepios Research Project, 2004 route des Lucioles, 06902 Sophia-Antipolis, France. Tel.: +33 (0) 492387811.

E-mail addresses: nicolas.toussaint@kcl.ac.uk (N. Toussaint), stoeck@biomed.ee.ethz.ch (C.T. Stoeck), tobias.schaeffter@kcl.ac.uk (T. Schaeffter), kozerke@biomed.ee.ethz.ch (S. Kozerke), maxime.sermesant@inria.fr (M. Sermesant).

1361-8415/$ - see front matter © 2013 Elsevier B.V. All rights reserved.
http://dx.doi.org/10.1016/j.media.2013.02.008

Please cite this article in press as: Toussaint, N., et al. *In vivo* human cardiac fibre architecture estimation using shape-based diffusion tensor processing. Med. Image Anal. (2013), http://dx.doi.org/10.1016/j.media.2013.02.008

In this article, we propose to use a coordinate system known as Prolate Spheroidal coordinates in order to generate a curvilinear scheme for data analysis and dense approximation of the fibre architecture of the Left Ventricle (LV). A preliminary version of this work was published in Toussaint et al. (2010).

The contributions of this work are twofold: first a conformal mapping method that allows the description of acquired tensor data in the LV wall into a normalised Prolate Spheroidal (PS) frame is introduced, using non-linear registration and PS coordinate change. Second, a dense approximation scheme in this PS frame is proposed, using a tri-variate kernel regression in order to approximate tensors at all locations in the LV from sparsely acquired data. It is demonstrated that using PS coordinates allows meaningful interpretation of data in the LV, in particular the orientation of the underlying fibres. Moreover, it is shown that changing the coordinate system from Cartesian to PS leads to better overall approximation of the global tensor field. These techniques are tested on a high resolution *ex vivo* DTI dataset, and applied to a set of *in vivo* data acquired on 5 healthy volunteers.

2. Material and methods

2.1. Ex vivo high resolution cardiac DTI dataset

An *ex vivo* DTI dataset of a healthy human myocardium was downloaded from the John Hopkins University website.[1] It was provided by Prof. Patrick A. Helm and Raimond L. Winslow at the Centre for Cardiovascular Bioinformatics and Modelling and Prof. Elliot McVeigh at the National Institutes of Health. Data was acquired on a 1.5T GE CV/I MRI Scanner (General Electrics Medical System), with a spatial resolution of $0.4297 \times 0.4297 \times 1.0\ \text{mm}^3$.

2.2. In vivo cardiac DTI acquisition

Cardiac DTI was performed on five healthy subjects (two males, three females) on a 1.5 T clinical MR scanner (Philips Heathcare, Best, The Netherlands) equipped with a gradient system with maximal strength of 80mT/m and a slew rate of 100 mT/m/ms per axis. A 32 channel cardiac coil array was used for signal reception. The imaging protocol consisted of a B0 map for image based shimming (Schär et al., 2004), a trigger delay scout sequence for estimation of optimal trigger points during systolic contraction (Stoeck et al., 2011), the actual DTI acquisition and a single breath hold 3D T2 contrast enhanced whole heart acquisition. All sequences were ECG-triggered, and Diffusion Weighted Images (DWIs) were acquired during free breathing using a respiratory navigator, with a gating window of 5 mm, placed on the right hemidiaphragm. DTI acquisitions were planned in short axis view of the heart and 4–6 parallel slices were acquired along the long axis of the LV. Imaging was performed using a diffusion weighted spin echo sequence with single shot echo planar imaging (EPI) readout (see Fig. 1). Imaging parameters were as follows: Echo Time (TE)/Repetition Time (TR) 59 ms/2R–R intervals, Field Of View (FOV): $230 \times 102\ \text{mm}^2$, in-plane resolution: $2 \times 2\ \text{mm}^2$, slice thickness: 5 mm. The Diffusion Weighted MR sequence is illustrated in Fig. 1.

In order to operate with a single DTI acquisition protocol in all volunteers, a TR of two R–R intervals was chosen to assure a sufficiently high SNR of each single shot DWI. Readout and echo time was shortened by using a rectangular FOV (local-look), applying the excitation pulse in phase encoding direction and the refocusing pulse in slice-select direction (Gamper et al., 2007). Furthermore a partial Fourier coefficient of 0.63 was used and the echo pulse duration was further shortened by applying the variable rate selective excitation (VERSE) technique (Hargreaves et al., 2004). Diffusion encoding was achieved by two bipolar gradients (Dou et al., 2003) applied in 18 directions distributed on the unit sphere, creating a *b*-value of 500 s/mm^2. Ten averages were acquired for each diffusion encoding direction. The total scan time was 10–15 min per DTI slice, depending on navigator efficiency.

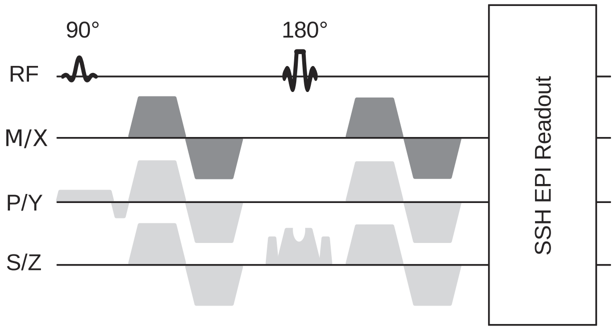

Fig. 1. DTI spin echo pulse sequence with single shot EPI readout. Diffusion encoding is established with a pair of velocity compensating bipolar gradients. For local look imaging, the excitation pulse is applied in phase encoding direction, while the echo pulse remains in slice-select direction. The echo pulse duration is shortened using VERSE.

A 3D whole heart acquisition using a T2 contrast prepared multi-shot gradient echo sequence with a resolution of $2 \times 2 \times 4\ \text{mm}^3$ was acquired directly after the Diffusion acquisitions, in order to ensure alignment between the DTI and the anatomical data. The trigger delay of the whole heart acquisition was set identical to the trigger delay of the diffusion weighted imaging.

Despite the respiratory navigation, residual misalignments, on the order of 2–3 mm, can occur between DWIs. This is corrected prior to averaging per direction using an approach very similar to the one detailed in Oubel et al. (2012): each DWI S_i is rigidly registered to an arbitrary chosen reference image S_r^k, using the Mutual Information similarity metric, resulting in a rigid transformation A_i^k. The mean diffusion image between all transformed S_i is computed and serves as a reference S_r^{k+1} for the following registration iteration. In this $(k+1)$ iteration, the transformations A_i^k are used as initialization for the registration algorithm, therefore avoiding successive resampling of the initial DWIs S_i. The operation is repeated until the mean square error (MSE) between two consecutive iterations is lower than a small threshold ϵ: $MSE\left(S_r^{k+1}, S_r^k\right) < \epsilon$. In practice five iterations were sufficient for convergence.

Tensors were reconstructed in each voxel by solving the Stejskal–Tanner's diffusion equation system (Stejskal and Tanner, 1965) using linear regression as described in Basser et al. (1994). Only tensors lying within the LV compact myocardium were considered for further processing. Illustrations of the acquisitions are presented in Fig. 2.

2.3. Conformal mapping of left ventricular data

In this section we describe a method to represent DTI information contained in the LV wall into a common reference frame. This is achieved with the use of the PS curvilinear coordinate system. It involves a non-linear registration of the LV wall onto a truncated ellipsoid, and a change of coordinate.

2.3.1. Prolate spheroidal coordinates

The LV wall is a relatively thin and non-convex structure with a shape close to an ellipsoid. The PS coordinates are well adapted to such an object, and have the advantage to be physiologically meaningful with respect to the ventricular shape and fibre architecture

---

[1] http://www.ccbm.jhu.edu/research/DTMRIDS.php.

Please cite this article in press as: Toussaint, N., et al. *In vivo* human cardiac fibre architecture estimation using shape-based diffusion tensor processing. Med. Image Anal. (2013), http://dx.doi.org/10.1016/j.media.2013.02.008

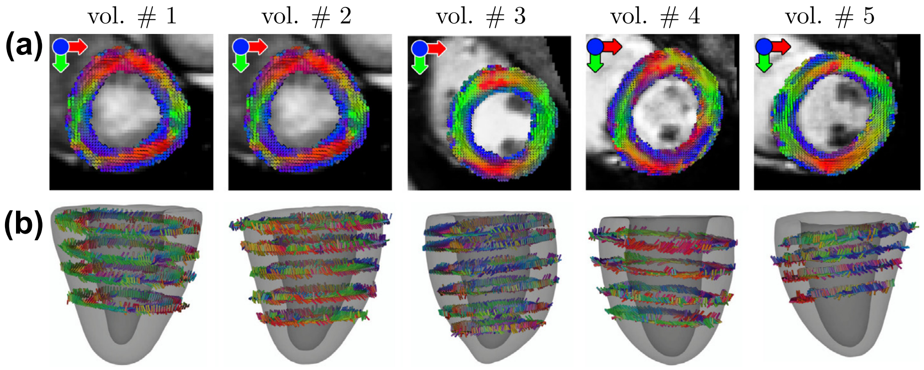

Fig. 2. Acquired volunteer data. (a) One slice of diffusion tensors. Tensors are colour-coded according to the direction of their main eigenvector, i.e. red: horizontal/green: vertical/blue: through-plane. (b) Distribution of the slices for each volunteer, super-imposed onto the Left Ventricle (LV) segmentation. (For interpretation of the references to colour in this figure legend, the reader is referred to the web version of this article.)

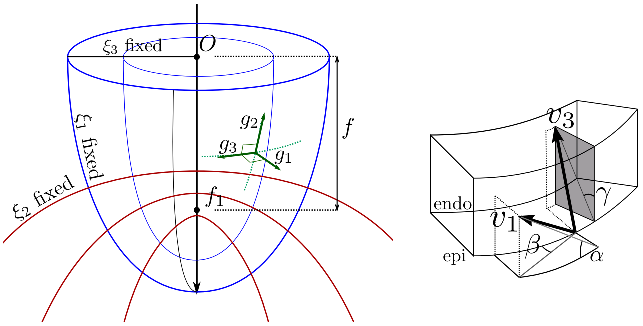

Fig. 3. Left: PS coordinate system depends on an arbitrary ellipsoid centre and semi-foci distance. The iso-lines of constant coordinates are drawn to illustrate its relevance for the ventricular shape. Right: definition of helix (α), transverse (β) and sheet (γ) angles with respect to the tensor's first (v_1) and third (v_3) eigenvectors.

(Nielsen et al., 1991; Costa et al., 1996; LeGrice et al., 2001; Rohmer and Gullberg, 2006).

The transformation operator from Cartesian coordinates $x = (x_1, x_2, x_3)^T$ to PS coordinates $\xi = (\xi_1, \xi_2, \xi_3)^T$ is denoted $\Psi: x \rightarrow \xi = \Psi(x)$. However, it is more commonly given in its inverse form Ψ^{-1}:

$$\begin{cases} x_1 = f\sinh(\xi_1)\sin(\xi_2)\cos(\xi_3) \\ x_2 = f\sinh(\xi_1)\sin(\xi_2)\sin(\xi_3) \\ x_3 = f\cosh(\xi_1)\cos(\xi_2) \end{cases} \quad (1)$$

where f is the semi-foci distance.

The first coordinate ξ_1 is strictly positive and can be interpreted as the transmural depth, ξ_2 as the long axis abscissa going from 0 at the apex to $\sim\pi/2$ at base level, and ξ_3 as a circumferential abscissa from 0 to 2π. In the common Cartesian system, the contravariant basis is stationary in $\mathbb{R}^3$. The PS equivalent, here denoted $\mathcal{G} = (g_1, g_2, g_3)$ (where $g_i = \frac{\partial x}{\partial \xi_i}$) varies in space, following the natural shape of the ventricle (see Appendix B for explicit expression of contravariant vectors).

PS coordinates have the advantage of describing the highly non-convex volume of the ventricle walls as a parallelogram, as shown in Fig. 4. In the PS frame, the shortest path from two distinct points of the ventricle remains in the ventricle. Therefore, a metric defined in this frame becomes *geodesically convex*.

2.3.2. Diffeomorphic registration

In order to ensure that the curvilinear coordinate system follows the shape of the anatomical LV, the imaged ventricle has to be registered to a perfectly shaped truncated ellipsoid volume. The source and target images S and T of this registration step are respectively the binary mask of the segmented LV and the binary mask of a corresponding approximated truncated ellipsoid volume. Fig. 5 shows a superposition of delineations of the masks S and T onto the anatomical image. S is obtained by manual segmentation of the myocardium using the 3D anatomical image. The volumetric truncated ellipsoid T was computed as the closest to the segmentation S, using the centre of mass and main axis of symmetry of S.

The non-linear algorithm used to register S to T is the symmetric version of the log-domain diffeomorphic demons (Dru and Vercauteren, 2009). This algorithm has the crucial characteristic to provide invertible displacement fields, needed to produce forward and backward transformation between the subject's anatomy and the volumetric truncated ellipsoid. Transformations are respectively denoted Φ and Φ^{-1}. Additionally, the displacement was constrained to be elastic (but yet compressible) as described in Mansi et al. (2011), in order to obtain a smooth displacement of the middle-wall area, where no texture is present in the masks to guide registration. This technique provides forward and backward transformations between the volunteer's anatomy and a volumetric truncated ellipsoid.

2.3.3. Transformation workflow

Once the LV of the subject is transformed onto the perfectly shaped truncated ellipsoid volume T using transformation Φ, the operator Ψ can be used to express this information in PS coordinates. Transformation from Cartesian to PS coordinates is defined by inverting the system in Eq. (1). Details of the inversion are given in Appendix A.

The overall transformation process towards a common PS frame can be summarised as follows:

$$\xi = \Psi \circ \Phi(x) \quad (2)$$

The operators Φ and Ψ are fully invertible, apart from the singularity segment (see Appendix A). As a consequence, it is possible to transform any LV input data into the PS frame, process it in a well adapted coordinate system, and transform it back to the anatomical reference.

The global transformation process of this conformal mapping is illustrated in Fig. 6. The anatomical left ventricular wall volume Ω is transformed to the convex box Ω'' that is the PS frame. A natural path lying within the LV wall (dotted lines in Ω) becomes a straight line in Ω''. Therefore, any process, such as interpolation or geodesic distance definition, described in PS frame will follow the natural shape of the LV.

Extension to tensor data: In our work, the type of data under consideration is not scalar but consists of tensors. Adjustments to the transformation operators Φ and Ψ are needed in order to

Please cite this article in press as: Toussaint, N., et al. *In vivo* human cardiac fibre architecture estimation using shape-based diffusion tensor processing. Med. Image Anal. (2013), http://dx.doi.org/10.1016/j.media.2013.02.008

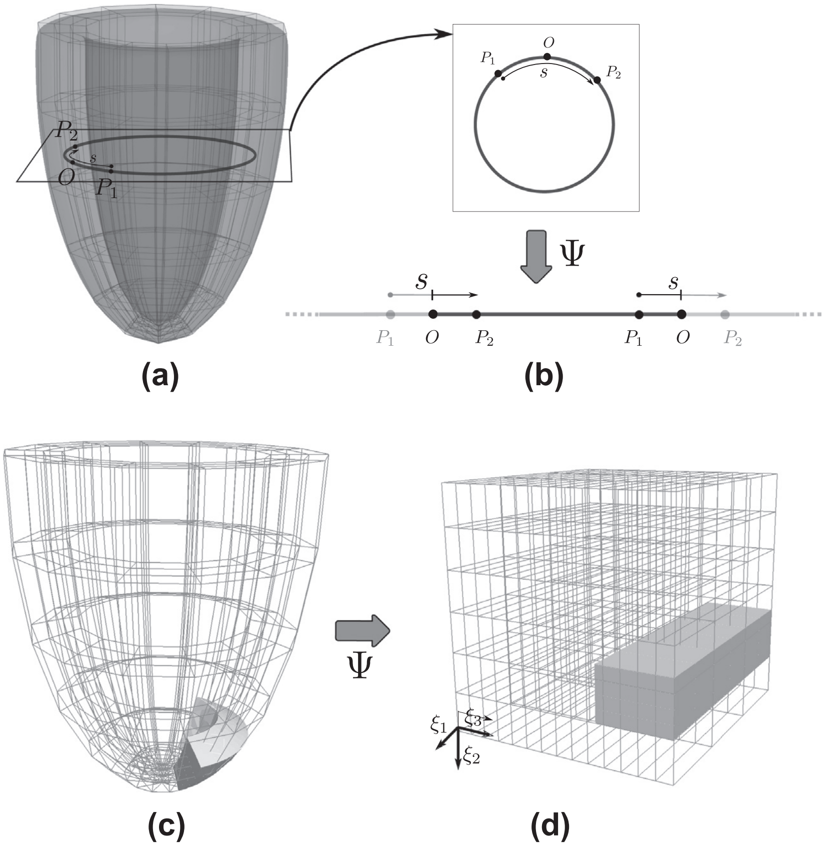

Fig. 4. (a,b): A short axis circle drawn in the Cartesian space (a) is represented as a segment in the Prolate Spheroidal (PS) frame (b). ξ_3 being defined with a modulo, the segment is reproduced at infinity on both sides, and the barycentre of P1 and P2 remains O. (c,d): A left ventricle volume is non-convex in a Cartesian frame (c) whereas the same volume expressed in a PS frame becomes a convex box (d).

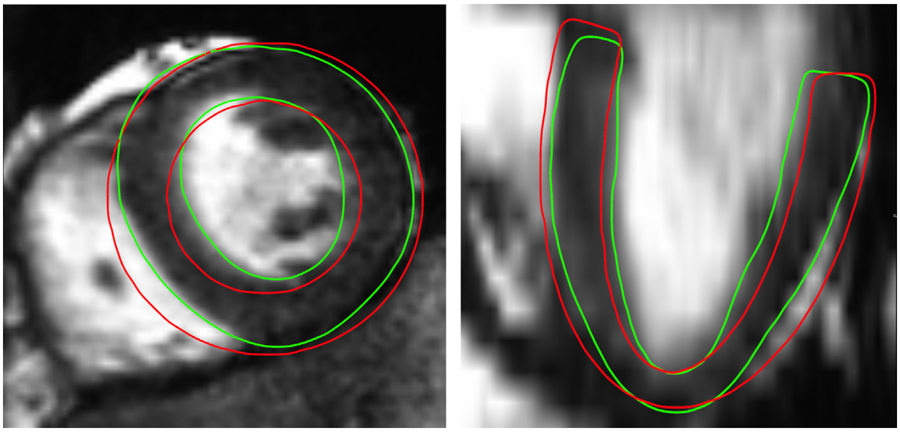

Fig. 5. Binary mask *S* of the acquired left ventricle (in green) obtained by manual segmentation. From the centre of mass and main axis of revolution of *S* is derived the closest volumetric truncated ellipsoid mask *T* (in red). (For interpretation of the references to colour in this figure legend, the reader is referred to the web version of this article.)

account for that increased data dimensionality. Let us denote $\widetilde{\Phi}$ the *induced* transformation from Φ on tensors. Transforming the diffusion tensors implies a reorientation scheme using the Jacobian $\mathcal{J}_{\Phi^{-1}}$ (in our case directly available from Φ^{-1}). In Peyrat et al. (2006), two different reorientation strategies are compared: The Finite Strain (FS) method separates the deformation in a rigid rotation and a pure deformation one, and only applies the rotation $\widehat{\mathcal{J}}_{\Phi^{-1}}$ to the tensor. The Preservation of Principal Direction (PPD) method takes the full Jacobian to reorient the tensor. The study concludes that FS is best suited for preserving the geometrical properties of diffusion tensors in this context. The FS strategy was chosen for this reason and its computational efficiency.

Similarly, extending the change of coordinate to tensors requires the *induced* transformation of the operator Ψ. The Jacobian of Ψ corresponds to the contravariant basis $\mathscr{G}$ (Eq. (B.1)). This matrix is orthogonal by definition (PS coordinates is an orthogonal coordinate system), but not orthonormal. The norm of the contravariant vectors correspond to the scale factors of the coordinate system, which are the local derivatives $h_i = \partial x / \partial \xi_i$ (see Appendix B). In our setting, the domain of definition is a volumetric ellipsoid

Please cite this article in press as: Toussaint, N., et al. *In vivo* human cardiac fibre architecture estimation using shape-based diffusion tensor processing. Med. Image Anal. (2013), http://dx.doi.org/10.1016/j.media.2013.02.008

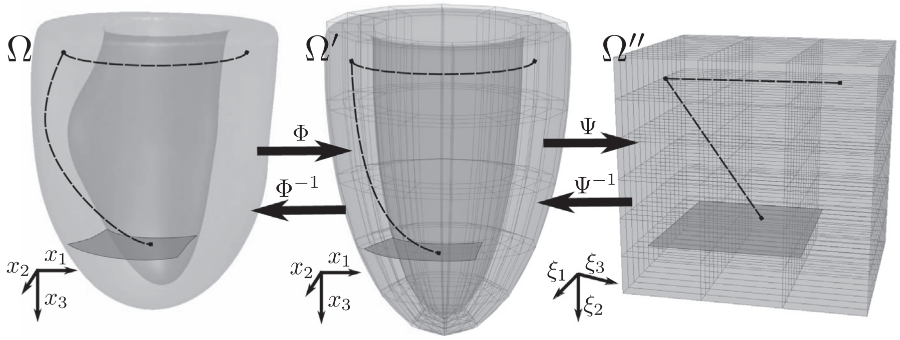

Fig. 6. Data transformation throughout the procedure. The anatomical LV (Ω) is registered onto a truncated volumetric semi-ellipsoid (Ω') with the displacement field Φ. The change of coordinate system from Cartesian to PS is performed with the operator Ψ, which results in a convex representation of the ventricular volume (Ω'').

Ω', and factors h_i vary spatially within the domain. In particular, they decrease with the distance to the long-axis. Therefore, taking the full Jacobian of Ψ to reorient the tensors and performing interpolation in the PS frame would privilege tensors of endocardial regions against epicardial ones, which is not desirable. For this reason, only the rotational component of $\widetilde{\Psi}$ is used: let us denote $\widehat{\mathscr{G}}$ the matrix constructed from the normalised column vectors of $\mathscr{G}$, using the scale factors h_i. Recalling that $\mathscr{G}$ is direct and orthogonal, $\widehat{\mathscr{G}}$ has therefore by construction a determinant equal to 1. Eq. (2) is rewritten with the induced transformations on tensors:

$$\xi = \Psi \circ \Phi(x) \quad \text{and } D_\xi = \widetilde{\Psi} \circ \widetilde{\Phi}(D_x)$$
$$\text{with : } \begin{cases} \widetilde{\Phi} : D \rightarrow \widetilde{\Phi}(D) = \widehat{\mathscr{J}}^T_{\Phi^{-1}} \cdot D \cdot \widehat{\mathscr{J}}_{\Phi^{-1}} \\ \widetilde{\Psi} : D \rightarrow \widetilde{\Psi}(D) = \widehat{\mathscr{G}}^T \cdot D \cdot \widehat{\mathscr{G}} \end{cases} \tag{3}$$

The induced transformations $\widetilde{\Phi}$ and $\widetilde{\Psi}$ both represent the finite strain transformations of tensors under Φ and Ψ.

Normalisation of the PS frame: For any PS position ξ, the third component ξ_3 is defined between 0 and 2π. The 0 position is imposed to be the intersection between the anterior wall and the Right Ventricle (RV). Similarly, the second component ξ_2 is normalised by construction between 0 at the apex and ξ_2^{base} at the basal region. The value ξ_2^{base} depends on where the base was in the manual segmentation S. The first component ξ_1, on the other hand, is not naturally normalised as it varies as a hyperbolic cosine. The upper and lower limit values of ξ_1 depend on both the radius of the LV and its thickness.

Data accumulation: The transformation scheme presented in Eq. (3) can be applied to DTI datasets of several subjects. All resulting sets of data are then described in a singular normalised PS frame, and can be combined in order to perform comprehensive groupwise analysis. This combination of data sets will further be referred to as $\mathscr{A}$. As DTI tensors are expressed in the PS contravariant basis $\mathscr{G}$, it becomes straightforward to derive meaningful information such as a measure of deviation of their main eigenvector from circumferential direction (projection on g_3). Circumferential, transmural and apico-basal variations of any information also become straightforward to express given the definition of the coordinate system.

2.4. Kernel-based DTI dense approximation from sparse data

In this section the approximation of a dense 3D tensor field from a set of sparse DTI measurements distributed across the ventricle is considered. Considering an input set P of M measured positions (or data centres) and tensors $P = (X_i, D_{X_i})_{i \in M}$, the approximation operator $\mathscr{W}_P$ is defined over a domain Σ (e.g. covering the ventricular wall volume), that describes how to recover data at position X from noisy and scattered input data:

$$\forall X \in \Sigma, \quad D_X := \mathscr{W}_P(X) \tag{4}$$

where Σ refers to the spatial target domain where samples are needed. It can be of lower or higher cardinality than P and may not be necessarily defined on a regular grid nor constrained within the convex hull of P. Solutions to approximate missing data and data fitting have been explored in the past. For instance, in Fillard et al. (2005), the authors used Radial Basis Functions (RBFs) in order to find a smooth solution for $\mathscr{W}_P$ that satisfies the interpolant constraint. However, because input data can be corrupted by significant noise, we intentionally chose not to satisfy the interpolation condition. That is, the *approximation* operator (or quasi-interpolant) was considered rather than a rigorous *interpolation* operator. An interpolation operator gives back the input data at measure points (i.e. $\mathscr{W}_P(X_i) = D_{X_i}$), whereas a quasi-interpolant can approximate results ($\mathscr{W}_P(X_i) \neq D_{X_i}$). Methods to regularise noise corrupted tensor fields have been proposed in the literature (Fillard et al., 2007; Frindel et al., 2009). In the present method the regularisation is integrated into the approximation operator: the operator $\mathscr{W}_P$ consists of taking a weighted mean of surrounding tensors as an estimate. To avoid swelling effect on tensors and to address the fact that the spatial density of P can be low in the practical case, the mean in the log-Euclidean sense (Arsigny et al., 2006) was used. Other metrics meeting those requirements could be used, such as in Yang et al. (2012) for instance, where a tensor is described by its eigenvalues and orientation features. The approximation operator is therefore written as follows:

$$\mathscr{W}_P : X \rightarrow \mathscr{W}_P(X) = \exp\left(\frac{\sum_{i=1}^{N} K(X - X_i)\log(D_{X_i})}{\sum_{i=1}^{N} K(X - X_i)}\right) \tag{5}$$

K is a vector to scalar function ($\mathbb{R}^3 \rightarrow \mathbb{R}$). In our setting, the kernel K is tri-variate and not necessarily isotropic:

$$K_H : dX \rightarrow K_H(dX) = \det(H)^{-1} k\left(\sqrt{dX^T H^{-2} dX}\right)$$

where H is a 3×3 diagonal matrix that needs to be optimised (Härdle and Marron, 1985). The function k is a given univariate kernel function. In this work, the Normal Gaussian function was chosen for k: $k(s) = (2\pi)^{-1/2} \exp(-s^2/2)$. Diagonal values of H therefore control the smoothness of the resulting approximation in the considered coordinate frame.

The approximation operator in Eq. (5) is applied on the set of acquired data centres $P'' = (\xi, D_\xi)$ in the PS frame, therefore enforcing spacial coherence independently in each of the main directions of the heart anatomy (e.g. radial, longitudinal and circumferential in PS coordinates). It is important to note that $\Psi \circ \Phi$ also needs to be applied to each position x of the target domain Ω where estimates are needed. Each resulting estimate $\mathscr{W}_P(\xi)$ is eventually transformed back to Cartesian coordinates and warped back to

Please cite this article in press as: Toussaint, N., et al. *In vivo* human cardiac fibre architecture estimation using shape-based diffusion tensor processing. Med. Image Anal. (2013), http://dx.doi.org/10.1016/j.media.2013.02.008

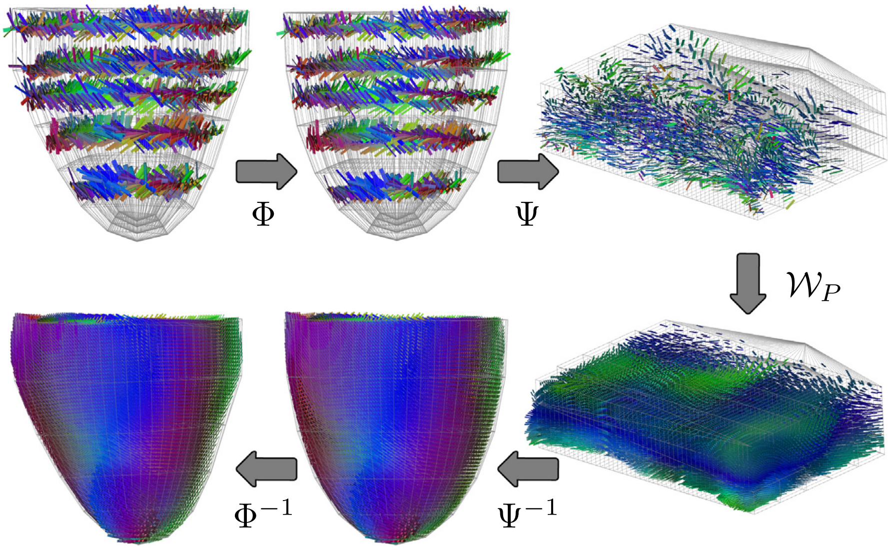

Fig. 7. Global data workflow, from a set of acquired DTI slices towards the full ventricular approximated tensor field. The PS conformal mapping is materialised by the operators Φ and Ψ. The dense approximation is materialised by the operator $\mathscr{W}_P$. All operators are fully invertible and diffeomorphic, apart from $\mathscr{W}_P$.

the initial geometry using inverse transformation operators Ψ^{-1} and Φ^{-1}. The global transformation process is summarised in Fig. 7, and the approximation operator can be written as:

$$\mathscr{W}_P(x) = \Phi^{-1} \circ \Psi^{-1} \circ \mathscr{W}_P(\xi) \tag{6}$$

2.5. Implementation

The segmentation of the ventricles was performed using the CardioViz3D software (Toussaint et al., 2008). The registration between the segmented LV and the truncated ellipsoid was done with the implementation available in Dru and Vercauteren (2009), with the addition of the elasticity constraint as detailed in Mansi et al. (2011). The tensor estimation as well as the tractography results were obtained using the Tensor ToolKit library,[2] which implements methods described in Fillard et al. (2007). Visualisation of tensor fields and fibre fields were obtained using the vtkINRIA3D software (Toussaint et al., 2007). All algorithms concerning the conformal mapping and the dense approximation were developed in a C++ITK-VTK based framework, and have been made available as an open-source library, the Cardiac Prolate Spheroidal ToolKit.[3]

3. Experiments and results

3.1. In vivo group-wise analysis

In this experiment the conformal mapping as detailed in Section 2.3 was applied to the set of *in vivo* DTI data obtained in healthy volunteers (see Section 2.2) in order to extract meaningful fibre orientation information. Transformations in Eq. (3) were applied to each of the subject datasets. The log-demons registration parameters were as follows: the velocity field diffusion-like regularisation σ was 2.5 mm, the Poisson ratio κ controlling the degree of global elasticity was $\kappa = 0.8$ (Eq. 9 in Mansi et al. (2011)), and the number of iterations in the multi-resolution scheme was $15 \times 10 \times 5$. Transformations resulted in a combined dataset $\mathscr{A}$ containing 18,350 data centres expressed in the PS frame. Coherency between ellipsoids was ensured by imposing that the plane ($\xi_3 = 0$) coincides with the junction between the LV and the RV at the anterior wall region. Boundaries of the first component ξ_1 were measured in each dataset, obtaining the following limits: $[0.35 \pm 0.02 \sim 0.55 \pm 0.03]$. The basal upper bound of ξ_2 was also measured $\left(\xi_2^{base}\right)$, obtaining a value of 107 deg ± 4. A normalisation of the first and second components ξ_1 was therefore applied to $\mathscr{A}$, with a target range corresponding to the mean of the measured limits. Fig. 8 presents the accumulated dataset $\mathscr{A}$. As $\mathscr{A}$ is expressed in PS coordinates, it is not convenient to visualise in this form. The operator Ψ^{-1} was therefore applied in order to transform $\mathscr{A}$ back to Cartesian coordinates, where it is then contained in the truncated ellipsoid Ω'. This figure shows an overall good coverage of the ventricle. As predicted, the area close to the apex is poorly populated due to the challenge of the acquisition in this part of the LV. The non-linear motion involved in this region makes the

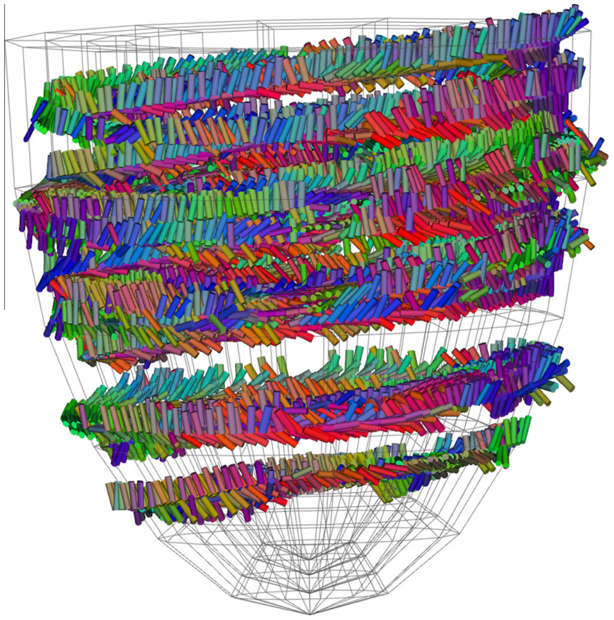

Fig. 8. All volunteers data was registered and mapped to a common PS frame. This illustration shows the accumulation of the datasets (denoted $\mathscr{A}$) in the template truncated ellipsoid volume. Tensors are shown as segments pointing to their first eigenvectors. The total amount of slices was 23 and the total amount of data centres was 18,350.

---

[2] https://gforge.inria.fr/projects/ttk.

[3] https://github.com/ntoussaint.

Please cite this article in press as: Toussaint, N., et al. *In vivo* human cardiac fibre architecture estimation using shape-based diffusion tensor processing. Med. Image Anal. (2013), http://dx.doi.org/10.1016/j.media.2013.02.008

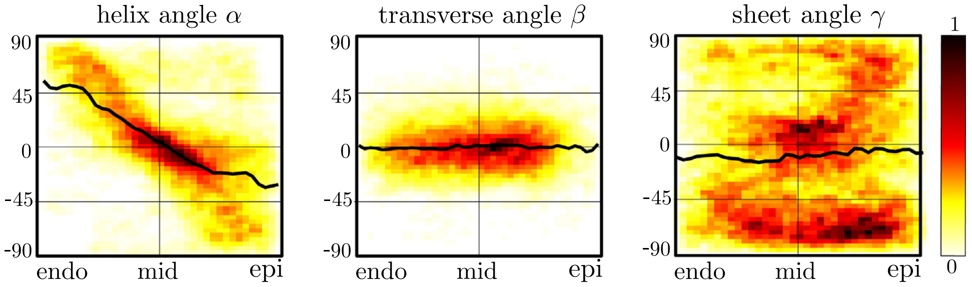
helix angle α transverse angle β sheet angle γ

Fig. 9. Joint histograms of respectively the helix α, transverse β, and sheet γ angles with respect to the transmural depth. Angles were derived from the projections of the tensors D_ξ onto the Prolate contravariant basis. The helix angle shows a variation between +55 deg at the endocardium to -30 deg at the epicardium.

acquisitions not representative of the actual anatomical fibre structure.

Three different angles of interest were then extracted from the acquired *in vivo* tensors of $\mathscr{A}$. As described in Fig. 3, the helix angle, denoted α, is the signed angle between the tensor's main eigenvector v_1 and the transmural short axis plane (g_1, g_3). Its variation with respect to the transmural depth (ξ_1) is of particular interest as it follows a recognisable pattern on healthy subjects as depicted *ex vivo* (Scollan et al., 2000; Lombaert et al., 2011a). The transmural angle β is the signed angle between v_1 and the wall surface (g_2, g_3). The laminar structure of the myocardial fibres can also be described by the DTI information (Helm et al., 2005). The plane defined by the vectors v_1 and v_2 is believed to be parallel to the underlying laminar sheet (Kung et al., 2011). The sheet angle γ is defined as the signed angle between v_3 and the wall surface (g_2, g_3). A high absolute value of γ implies that the local laminar sheet is close to be parallel to the wall surface. These projections were directly available as the tensors D_ξ are already expressed with respect to the PS contravariant basis $\mathscr{G}$. Using the PS expression of the diffusion tensors, these angles are mathematically defined as follows:

$$\begin{cases} \alpha = \arcsin(v_1, g_2) \\ \beta = \arcsin(v_1, g_1) \\ \gamma = \arcsin(v_3, g_1) \end{cases} \tag{7}$$

Joint histograms of the helix, transverse and sheet angles of population gathered in $\mathscr{A}$ with respect to the transmural depth ξ_1 are presented in Fig. 9. The helix angle α was found to vary between +55 deg at the endocardium to -30 deg at the epicardium, with a correlation coefficient of 0.581. The transverse angle β was found stable along the transmural depth with a mean equal to 0, and has a consequently low correlation coefficient of 0.260. The sheet angle γ was poorly correlated with the transmural depth, with a coefficient of 0.012.

3.2. Dense approximation: parameter estimation

In this experiment the dense approximation scheme detailed in Section 2.4 was evaluated on an high resolution *ex vivo* human DTI dataset (see Section 2.1). The approximation operator depends on a 3×3 diagonal matrix H that describes the shape of the tri-variate kernel K_H used in the approximation operator $\mathscr{W}_P$. This experiment aims at finding the optimal kernel width H_{opt} to use depending on two acquisition parameters: the density of slices and the amount of noise in the data. This optimisation was achieved by minimising the discrepancy between measured tensor data D_{X_i} and corresponding estimate $\mathscr{W}_P(X_i)$, while keeping a certain degree of smoothness.

In order to simulate a sparse distribution of acquired slices, it was hypothesised that a typical *in vivo* cardiac DTI acquisition would consist of a limited amount of short axis (SA) slices with a certain degree of noise. Furthermore, these slices are usually constrained to the equatorial part of the ventricle as motion pattern and partial volume effects around the apex hamper acquisition of images with sufficient quality. In consequence, N SA equatorial slices from the *ex vivo* dataset were extracted while avoiding the apex and base boundaries, as shown in Fig. 10 (see Fig. 11).

In order to simulate noise in the data, each of the N slices was then transformed to a series of 6 DWIs, using the L_2 norm over the tensors as a baseline image and 6 non-collinear gradient orientations uniformly distributed on the sphere. Complex Rician noise (Gudbjartsson and Patz, 2005) of variance V was added to the DWIs, before tensor re-estimation.

The resulting noisy DTI slices were then used as input data for the approximation scheme detailed in Section 2.4 and the full ventricular tensor field was computed. The output was compared to the true tensor field in a voxel-wise manner. A similarity measure was used to optimise matrix H_{opt}, as a trade-off over the entire ventricle domain Ω between a Least Square (LS) term that describes the data fit and a smoothness term (Reg):

$$\begin{aligned} H_{opt} &= \underset{H \in Diag(3)}{\operatorname{argmin}} \, LS(H) + \lambda \cdot Reg(H), \\ \text{with} & \begin{cases} LS(H) = \sum_* dist(D_*, \mathscr{W}_P(*))^2 \\ Reg(H) = \sum_* \|\partial \mathscr{W}_P(*)\|^2 \end{cases} \end{aligned} \tag{8}$$

where $*$ refers to $x \in \Omega$ in Cartesian coordinates or $\xi \in \Omega''$ in PS coordinates, and λ to the scalar controlling the influence of the regularisation. Among different existing similarity measures between tensors (named *dist* in the formula), the Log-Euclidean metric distance (Arsigny et al., 2006) was chosen. That is, the Frobenius norm of the matrix-log difference: $dist(A, B) = \|\log(A) - \log(B)\|$. The smoothness term (or regularisation term) can be seen as an equivalent of the total variation of the tensor field, i.e. the squared norm of the tensor field gradient in the log domain: $\partial \mathscr{W}_P(*) = \nabla \log(\mathscr{W}_P(*))$. The parameter space of this minimisation problem therefore only consists of the three diagonal elements of the bandwidth matrix H. The minimisation of Eq. (8) was performed using a gradient-free multivariate optimisation scheme (Powell, 2008).

The regularisation parameter λ controls the influence of the tensor field smoothness in the estimation of the optimal matrix H_{opt}. A common technique used to choose its value is the L-curve method as described in Hansen (1992). The L-curve was computed, as well as its curvature for the set of variables ($N = 7$, $SNR = 10$) in order to find a suitable value for λ. The curvature of the L-curve was found almost constant. However, it indicated an inflexion point at $\lambda \sim 0.05$–0.1. The constant curvature might be explained by the fact that the system we try to solve is non-linear and does not correspond to a Tikhonov regularisation problem, as opposed to the

Please cite this article in press as: Toussaint, N., et al. *In vivo* human cardiac fibre architecture estimation using shape-based diffusion tensor processing. Med. Image Anal. (2013), http://dx.doi.org/10.1016/j.media.2013.02.008

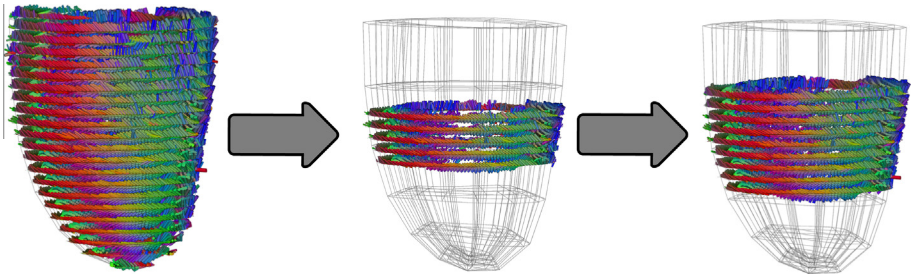

Fig. 10. Reference tensor field was downsampled and reoriented to obtain a voxel size of 2 × 2 × 4 mm^3 in a short axis slice orientation (left). The number of slices N was varied to simulate different *in vivo* acquisition situations.

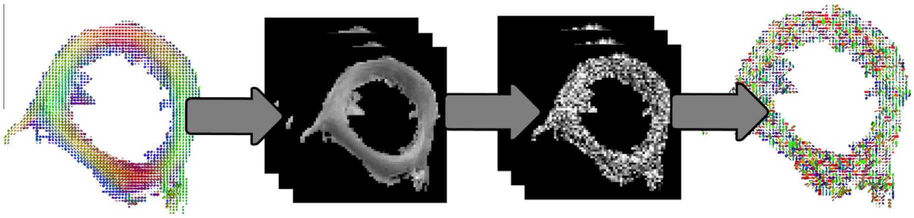

Fig. 11. 6 Diffusion Weighted Images (DWIs) were artificially computed from the reference tensor field. Each DWI was corrupted by additive Rician noise, and the tensor field was then estimated. The variance of the added Rician noise in this example was $V = 0.04$ for each DWI, which results in an SNR of 10.0.

system described in Hansen (1992).A value of $\lambda = 0.1$ was therefore used for all optimisation results described in this experiment.

For a better comprehension of the noise levels, the Signal to Noise Ratio (SNR) of the noisy DWIs was computed. A region of interest R was drawn in the exterior wall of one of the DWIs. Then the SNR was calculated as follows: $\text{SNR} = mean(R)/std(R)$. For instance, the reference *ex vivo* dataset used as a ground truth has a value of $\text{SNR}_0 = 36$.

The optimisation of the diagonal matrix H was performed for different case scenarios of values of N and values of SNR_V. The remaining residual error between the reference tensor field and the approximated one was computed. The error corresponds to the angle difference between main eigenvectors of the reference and the approximated tensor, denoted ε, in a voxel-wise manner. If ε is considered as a random variable, then it can be seen as the combination of two independent random variables that are the polar angular errors ε_1 and ε_2. To be calculated, those polar angular errors need the definition of two arbitrary planes going through the reference tensor's first eigenvector v_{1_r}, then ε_1 and ε_2 are the respective (signed) projections of the approximated tensor's first eigenvector v_{1_a} onto each of the planes, as shown in Fig. 12. Spherical trigonometry therefore infers that ε follows the distribution of arccos (cos ε_1 · cosε_2). An example of such distribution is simulated in Fig. 12. In this simulation ε_1 and ε_2 are chosen to have a zero-mean Gaussian distribution. The distribution of ε was calculated (shown in red in Fig. 12), it has a strongly skewed shape. The value of the mode (or peak) is therefore a good indicator of the most probable angular error, and of the performance of the approximation scheme.

Mode values of the residual error ε are reported in Fig. 13a. The two graphs show this mode value as a function of both the number of slices N and the SNR of the DWIs, when using Cartesian coordinates (left) and PS coordinates (right) for the approximation scheme. For instance, for the case scenario ($N = 7$, $\text{SNR} = 10$), mode values of 11.5 deg and 8.3 deg were found (grey and black dots in the figure). The corresponding values for the bandwidth matrix were $H_{opt}^{cart} = \text{diag}(3.3, 3.3, 5.9)$ (in mm) and $H_{opt}^{prol} = \text{diag}(0.009, 0.20, 0.31)$.

To visually evaluate the spatial distribution of the residual approximation error, we present in Fig. 13b the local distributions of ε along the ventricle for the specific case of ($N = 7$, $\text{SNR} = 10$). The grey rectangles represent the location of the seven input noisy DTI slices.

Additionally, fibre tractography was performed using the approximated dense tensor fields resulting from Cartesian and PS coordinates approaches in order to visually assess the impact of using the PS frame for interpolation. Fibres were tracked in a voxel-wise manner using a propagation term as described in Fillard and Gerig (2003), using an advection–diffusion propagation term derived from Weinstein et al. (1999). Fibre tractography results are presented in Fig. 14. For comparison, tractography was also applied to the initial fully sampled tensor field.

3.3. In vivo fibre tractography results

In this section, the dense approximation scheme was applied to each 5 individual *in vivo* datasets separately, and to the accumulated dataset $\mathscr{A}$, using optimal parameters H_{opt} as found in Section 3.2, in order to visually assess the resulting dense fibre orientations.

In order to choose adequate optimal bandwidth matrix for the dense approximation, the SNR and the ventricle coverage of the *in vivo* acquisitions were measured. The mean SNR was 10 and the mean ventricle coverage was of 40%. These measures were reported on the graphs in Fig. 13a (grey and black dots) and the corresponding diagonal values of H_{opt} were chosen for the dense approximation. The approximation scheme was then applied to each of the subject's datasets separately, as well as to the combined dataset $\mathscr{A}$, using PS coordinates. Resulting dense tensor fields were transformed back into Cartesian coordinates and to their respective anatomical geometry using operators Ψ^{-1} and Φ^{-1}. The resulting dense tensor fields are presented in Fig. 15a in a mid-ventricular short axis section. All obtained dense tensor fields were eventually used for fibre tractography for qualitative assessment of the resulting fibre orientations. Fibre tractography results for each subject are presented in Fig. 15b. For the special case of $\mathscr{A}$, there does not exist any corresponding anatomical geometry, i.e. there exists no anatomical template in our workflow. The resulting dense tensor field from $\mathscr{A}$ was therefore warped onto the geometry of volunteer # 3, and fibre tractography was performed. The result

Please cite this article in press as: Toussaint, N., et al. *In vivo* human cardiac fibre architecture estimation using shape-based diffusion tensor processing. Med. Image Anal. (2013), http://dx.doi.org/10.1016/j.media.2013.02.008

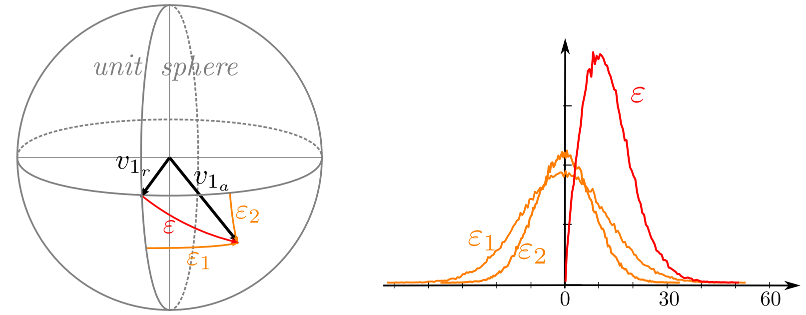

(a) Angular error ε as a combination of polar angles (b) Corresponding statistical distributions

Fig. 12. (a) Residual error ε due to the approximation scheme on the angle between the approximated tensor's first eigenvector v_{1_a} and that of the reference tensor v_{1_r}. ε can be seen as a combination of two independent polar signed angles ε_1 and ε_2. (b) If ε_1 and ε_2 have a zero-mean Gaussian distribution, then the distribution of ε is strongly skewed, and depends on the standard deviations of the polar angle errors.

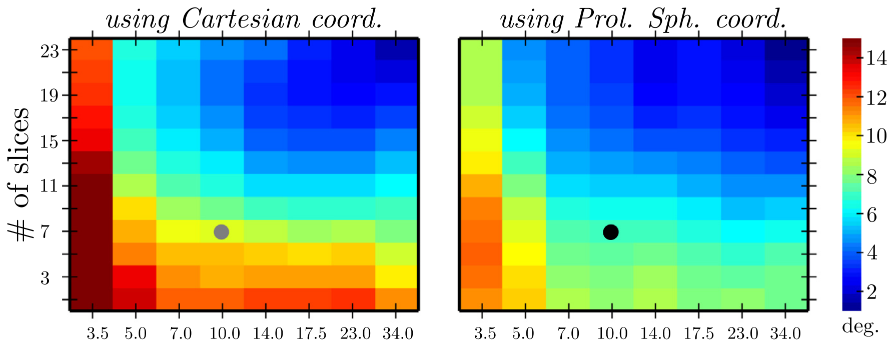

(a) Angular error mode function of input noise and # of slices

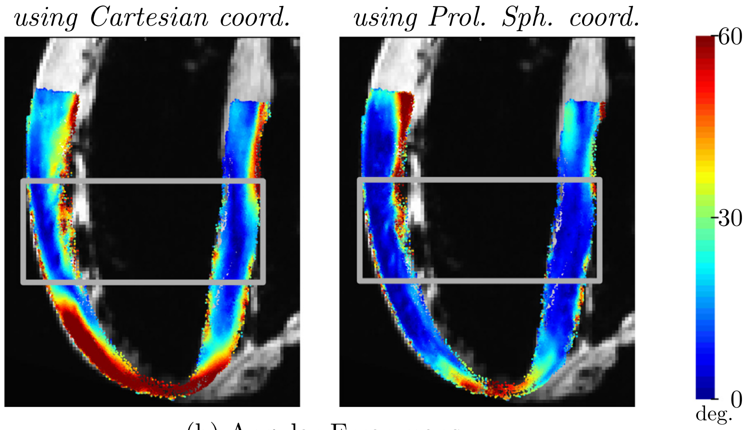

(b) Angular Error maps

Fig. 13. (a) Mode of the residual angular error ε of the approximation process showed as a function of both the number of slices N and the SNR of the DWIs. (b) Maps of the angular error for the case $N = 7$ and SNR = 10. Results are presented for both Cartesian (left) and prolate spheroidal (right) coordinates. Grey rectangle: region covered by the seven slices.

is presented in Fig. 15c, where the fibres are colour-coded with the local helix angle α.

4. Discussion

4.1. Group-wise study

The PS conformal mapping methodology described in this paper constructs a normalised referential for the LV from which DTI information can be analysed in a straightforward manner. Its application to an *in vivo* database of healthy subjects allowed to observe the global distribution of fibre orientation throughout the ventricle. As the accumulated dataset $\mathscr{A}$ is expressed in the PS frame, simple projections of the tensors D_ξ main eigenvectors on the contravariant basis $\mathscr{G}$ allowed for the extraction of local fibre orientation. A strong and linear negative correlation between the helix angle and the transmural depth was observed, confirming previous *ex vivo* studies. The reported range of +55 $\sim$ −30 deg (Fig. 9) is in relative agreement with values reported in the literature for *ex vivo* canine and human hearts (Streeter and Hanna, 1973; Scollan et al., 2000; Anderson et al., 2008). The value at

Please cite this article in press as: Toussaint, N., et al. *In vivo* human cardiac fibre architecture estimation using shape-based diffusion tensor processing. Med. Image Anal. (2013), http://dx.doi.org/10.1016/j.media.2013.02.008

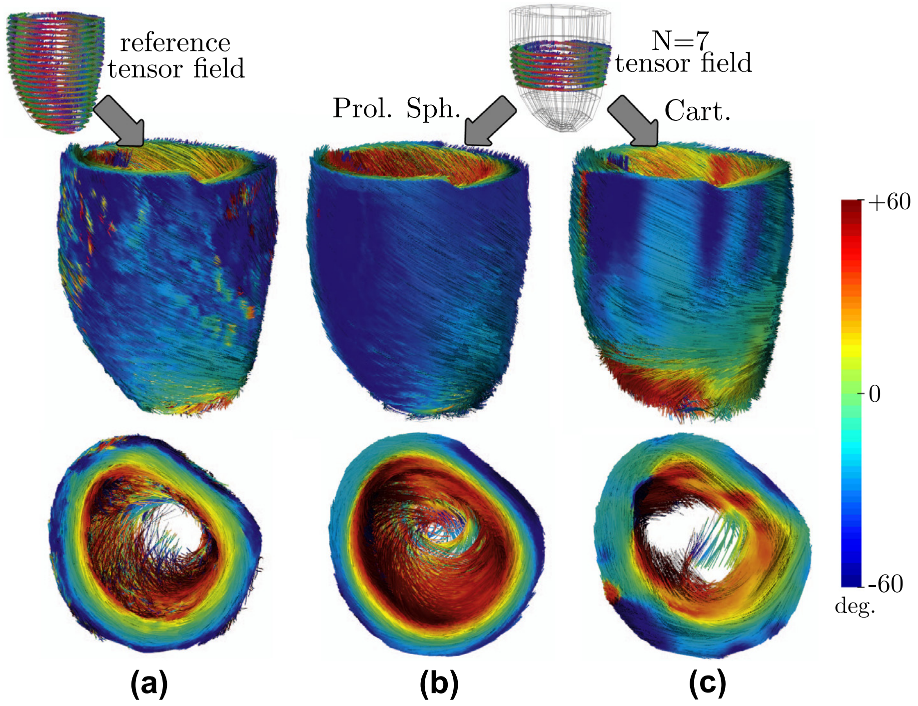

Fig. 14. (a) Tractography results from the reference fully sampled tensor field. (b,c) Tractography results from approximated tensor fields when using the noisy set of tensors ($N = 7$, SNR = 10), and using the PS approach (b) and Cartesian approach (c).

the endocardium is strongly influenced by the limit of the segmentation. Accordingly, one has to be careful not to include the papillary muscles of the LV in the segmentation as they tend to bias the elevation angle's endocardial limit by introducing vertical tensors in the computation. This consideration might partly explain the asymmetry of the ranges reported both in this experiment and in the literature. The transverse angle shows a stable mean value of zero along the transmural depth. This indicates that fibres are mostly oriented parallel to the wall surface, as also observed *ex vivo* in Lombaert et al. (2011a). On the other hand, the sheet angle does not seem to have a significant correlation with the transmural depth. Similar results were obtained e.g. in Lombaert et al. (2011b). A low correlation with the transmural depth does not necessarily mean the absence of features: a primary cluster can be seen at the high negative values all along the transmural depth, and a secondary cluster is situated close to zero at the mid-wall region. These clusters indicate that a majority of laminar sheets seem to be oriented parallel to the wall surface, and that some laminar sheets parallel to the short axis can be seen at mid-wall depth. Further investigation is needed to study the local laminar sheet structure rather than study its global variation along one axis.

4.2. Dense approximation and fibre tracking

The dense approximation scheme presented in this work takes advantage of the PS frame mapping in order to infer spatial coherency of the approximation along the natural shape of the ventricle. As demonstrated in Fig. 13 and 14, This approach shows better approximation accuracy when compared to the common Cartesian approach. The tensor fields and fibre architecture approximated from *in vivo* data (Fig. 15a and b) demonstrate a variation of fibre orientation from endocardium to epicardium that is in agreement with the expected structure as reported in the literature for *ex vivo* hearts (Scollan et al., 2000; Peyrat et al., 2006). The double helix pattern is observed on all datasets. Accumulating the datasets in $\mathcal{A}$ allowed us to appreciate the average fibre orientation structure among the population of this study (Fig. 15c), where the helical pattern of the fibres is observed.

4.3. Sensitivity to parameters

Segmentation: The anatomical shape of the ventricle was extracted using manual segmentation, and the closest truncated ellipsoidal volume was then computed from this segmentation. Segmentation errors might thus bias the study by including or excluding tensor information at the boundaries of the LV. As shown in Fig. 2, the endocardial boundary of the segmentation was carefully monitored to avoid the papillary muscles. The axis of rotation of the truncated ellipsoid is defined as the main axis of mass of the segmented LV. A variation of this axis will slightly impact the resulting statistical study. For instance, its effect on the graphs presented in Fig. 9 would be an increase/decrease of the vertical standard deviations of the angles α, β, and γ with no impact on the mean values. However, since a misevaluation of this axis by only 10 deg. at the base would already deviate the apex location by 1 cm, the error would be straightforward to pick during the process. In this case a manual adjustment of the axis becomes necessary to ensure a good overlap of the ellipsoid and the LV walls throughout the volume.

Registration: Additionally, errors could potentially be introduced by the diffeomorphic registration between the segmented ventricle and the truncated ellipsoid. Data centres and DTI information are transported to this ellipsoid simply for statistical analysis and interpolation purposes. Since tensors are reoriented according to the Jacobian of the transformation Φ, it can safely be said that only the rotation components of Φ can potentially bias the accuracy of the statistical results. It is therefore important that the segmentation is smooth to prevent for strong rotation components of the transformation Φ that would cause an anatomically incorrect extra rotation of the tensor information. In our experiments the displacement fields

Please cite this article in press as: Toussaint, N., et al. *In vivo* human cardiac fibre architecture estimation using shape-based diffusion tensor processing. Med. Image Anal. (2013), http://dx.doi.org/10.1016/j.media.2013.02.008

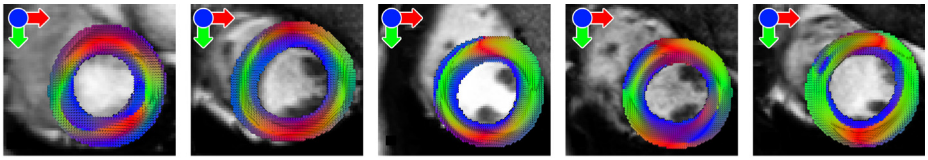

(a) short axis slice of the approximated tensor field for each volunteer

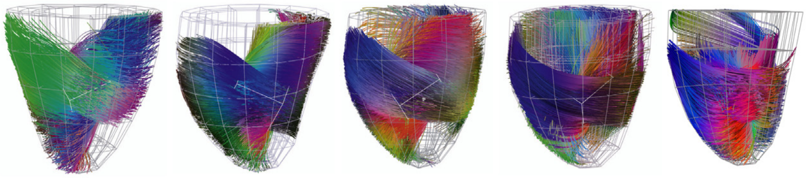

(b) Fibre reconstruction from the approximated tensor field for each volunteer

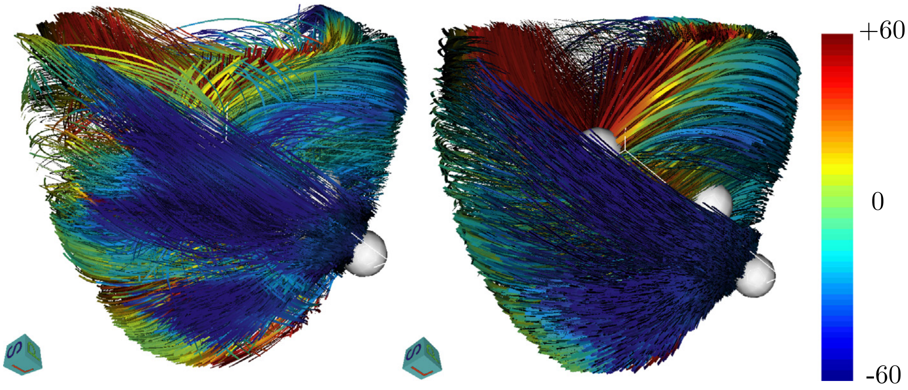

(c) Fibre reconstruction from the approximated tensor field of the cumulation of all datasets ($\mathcal{A}$), color coded with the helix angle α

Fig. 15. (a) Slice of approximated tensor field for each volunteer. (b) Part of the resulting fibre tracking illustrating the transmural helix angle variation. (c) Fibre tractography result from the accumulated dataset $\mathcal{A}$, using the Cartesian approach (left) and the PS frame approach (right). Fibres are colour-coded with the local helix angle α.

were found to be smooth with displacement vectors of the order of 1.28 ± 0.77 mm and Jacobian determinants of the order of 0.96 ± 0.06 (mean ± std).

Noise: The evolution of the error ε with respect to the addition of slices (each column of the error maps in Fig. 13a) seems to be significantly robust to noise. That is, the pattern was almost constant until reaching a SNR $\leqslant 5$. This is again explained by the relatively strong smoothness of the fibre orientation structure in a healthy left ventricle such as the one used as reference in this sensitivity analysis.

Smoothing: In the experiments shown in this work, a global kernel width matrix was used throughout the ventricle. Local variations in the acquired tensor dataset can be smoothed by this process. In the case of healthy subjects, this property might be desirable under the reasonable hypothesis that the fibre structure is relatively smooth. On the other hand, in clinical cases such as infarct subjects, the fibre architecture is suspected to be disoriented in the scar region. In this situation some more local approach would be necessary. For instance, one could consider using smaller kernel parameters in such regions in order to depict the fibre structure in more details. Tensor shape indices, such as the Fractional Anisotropy (FA) or the Spherical Coefficient (SC), could potentially be used as a detector of such regions in order to adjust the kernel parameters accordingly. As suggested in Yang et al. (2012), a metric on tensor which avoid FA collapse should be preferred in this situation.

5. Conclusion

This work demonstrates that human *in vivo* cardiac DTI is feasible in a reasonable acquisition time. The acquisition protocol that allowed such acquisition was described and applied to a set of 5 healthy volunteers. The methodological contributions of this work are twofold. First, a conformal mapping workflow was proposed for the analysis of cardiac DTI data in the left ventricular myocardium, that combines the use of the PS curvilinear coordinate system and a non-linear registration to a truncated ellipsoid. This workflow was applied *in vivo* to analyse the fibre orientation structure of the group of subjects. Results showed a structure in good agreement with those reported in the literature for *ex vivo* specimens. Second, an approximation scheme was presented to compute a 3D approximation of a dense tensor field from sparsely acquired DTI data. The performance of this scheme was demonstrated using a gold standard *ex vivo* dataset. It was then applied to the group of healthy volunteers. Resulting reconstructed dense fibre structure presents a visible double helical pattern in agreement with the cardiac anatomical knowledge.

The main advantage of this approach is the integration of the curvilinearity of the object of interest in the groupwise study and in the approximation process. This is particularly interesting when the data is sparsely distributed across the ventricle. The Riemannian metric induced by redefining the problem in PS coordinates becomes *geodesically convex*, which is a very desirable property in such processes.

Please cite this article in press as: Toussaint, N., et al. *In vivo* human cardiac fibre architecture estimation using shape-based diffusion tensor processing. Med. Image Anal. (2013), http://dx.doi.org/10.1016/j.media.2013.02.008

Future developments of the techniques introduced in this paper involve a local approach to the dense approximation scheme, where the kernel sizes would be adapted to the local coherence of the tensors. Such improvement could be used to depict and localise fibre disarray involved in scar patients, and potentially improve therapy planning in these cases.

Acknowledgements

The authors are extremely grateful to Dr. Tommaso Mansi for the help and source code of the elasticity constraint provided for the image registration, and to Prof. Nicholas Ayache for his constant support and many fruitful discussions. The authors wish to dedicate this work to Dr. Philip G. Batchelor.

Appendix A. Inversion of the prolate spheroidal transformation

Recalling the trigonometric and hyperbolic identities:

$$\cos^2 + \sin^2 = 1, \quad \text{and } \cosh^2 - \sinh^2 = 1$$

If the following notations is taken for Eq. (1):

$$A = f^2 \quad B = x_1^2 + x_2^2$$
$$C = x_3^2 \quad \alpha = \sin^2(\xi_2)$$

then, using first and second definitions from Eq. (1), and the trigonometric identity, we obtain:

$$B = A\sinh^2(\xi_1)\alpha \tag{A.1}$$

$\sinh^2(\xi_1)$ is a function of α, A, and C using the third definition from Eq. (1) and the hyperbolic identity, which eventually gives a polynomial in α:

$$A\alpha^2 + (-A + B + C)\alpha - B = 0 \tag{A.2}$$

Of the two roots of this polynomial, only one is positive. Noting that $\alpha = \sin^2(\xi_2)$ is positive by definition, only one root corresponds to the solution:

$$\sin^2(\xi_2) = \frac{(A - B - C) + \sqrt{(A - B - C)^2 + 4AB}}{2A}$$

Recalling that ξ_2 is an angle from 0 to π, $\sin(\xi_2)$ is always positive, and ξ_2 can then be extracted. ξ_1 is also a positive number by definition, and can therefore be extracted from Eq. (A.1) when $\sin^2(\xi_2) \neq 0$ (everywhere but on the axis of revolution). When $\sin^2(\xi_2) = 0$, one can use $\sinh^2(\xi_1) = C/A - 1$, which holds true everywhere on the axis apart between foci, where PS coordinates are undefined. Note that this singularity can be noticed directly from the third line of Eq. (1) and by recalling that $\cosh(*) \geqslant 1$. Indeed we then have $|x_3| > f$ required on the axis. In practice this singularity is never reached as it is always outside the ventricle wall. We can nevertheless extend the definition domain by its limit close to the axis of revolution, i.e. imposing $\xi_1 = 0$ in the segment between foci, rendering the singularity "removable".

Finally, ξ_3 is simply obtained by dividing second with first line of Eq. (1): $\xi_3 = \arctan(x_2/x_1)$, which holds true everywhere except at the axis of revolution. If the point is on the axis of revolution, ξ_3 can take any value between 0 and 2π. We use $\xi_3 = 0$ by convention.

Appendix B. Contravariant basis vectors

The PS contravariant basis $\mathcal{G} = (g_1, g_2, g_3)$, defines the differential vectors for each of the coordinates: $g_i = f\partial x / \partial \xi_i$.

$$g_1 = f\begin{pmatrix} \cosh(\xi_1)\sin(\xi_2)\cos(\xi_3) \\ \cosh(\xi_1)\sin(\xi_2)\sin(\xi_3) \\ \sinh(\xi_1)\cos(\xi_2) \end{pmatrix}$$

$$g_2 = f\begin{pmatrix} \mathit{sinh}(\xi_1)\cos(\xi_2)\cos(\xi_3) \\ \sinh(\xi_1)\cos(\xi_2)\sin(\xi_3) \\ -\cosh(\xi_1)\sin(\xi_2) \end{pmatrix}$$

$$g_3 = f\begin{pmatrix} -\sinh(\xi_1)\sin(\xi_2)\sin(\xi_3) \\ \sinh(\xi_1)\sin(\xi_2)\cos(\xi_3) \\ 0 \end{pmatrix} \tag{B.1}$$

The basis $\mathcal{G}$ is direct and orthogonal, but not orthonormal. The norm of each column vector is the inverse of the corresponding scale factor: $\|g_i\| = 1/h_i$.

The calculation of the scaling factors and the contravariant basis is involved in the "Finite Strain" reorientation for the induced transformation $\widetilde{\Psi}$, and the normalised basis is written $\widehat{\mathcal{G}} = \mathrm{diag}(h_i)\mathcal{G}$.

Appendix C. Supplementary material

Supplementary data associated with this article can be found, in the online version, at http://dx.doi.org/10.1016/j.media.2013.02.008.

References

Anderson, R.H., Smerup, M., Sanchez-Quintana, D., Loukas, M., Lunckenheimer, P.P., 2008. The three-dimensional arrangement of the myocytes in the ventricular walls. Clinical Anatomy 22, 64–76.

Arsigny, V., Fillard, P., Pennec, X., Ayache, N., 2006. Log-euclidean metrics for fast and simple calculus on diffusion tensors. Magnetic Resonance in Medicine 56 (2), 411–421.

Basser, P., Mattiello, J., LeBihan, D., 1994. Mr diffusion tensor spectroscopy and imaging. Biophysical Journal 66 (1), 259–267.

Basser, P., Pajevic, S., Pierpaoli, C., Duda, J., Aldroubi, A., 2000. In vivo fiber tractography using DT-MRI data. Magnetic Resonance in Medicine 44, 625–632.

Bovendeerd, P., Arts, T., Huyghe, J., van Campen, D., Reneman, R., 1992. Dependence of local left ventricular wall mechanics on myocardial fiber orientation: a model study. Journal of Biomechanics 25 (10), 1129–1140.

Costa, K.D., Hunter, P.J., Wayne, J.S., Waldman, L.K., Guccione, J.M., McCulloch, A.D., 1996. A three-dimensional finite element method for large elastic deformations of ventricular myocardium: II – Prolate spheroidal coordinates. Journal of Biomechanical Engineering 118 (4), 464–472.

Dou, J., Tseng, W.-Y.I., Reese, T.G., Wedeen, V.J., 2003. Combined diffusion and strain MRI reveals structure and function of human myocardial laminar sheets in vivo. Magnetic Resonance in Medicine 50, 107–113.

Dru, F., Vercauteren, T., 2009. An ITK implementation of the symmetric log-domain diffeomorphic demons algorithm. Insight Journal, 2009 January–June.

Fillard, P., Arsigny, V., Pennec, X., Ayache, N., 2007. Clinical DT-MRI estimation, smoothing and fiber tracking with log-Euclidean metrics. IEEE Transactions on Medical Imaging 26 (11), 1472–1482.

Fillard, P., Arsigny, V., Pennec, X., Thompson, P., Ayache, N., 2005. Extrapolation of sparse tensor fields: application to the modeling of brain variability. In: Christensen, G., Sonka, M. (Eds.), Information Processing in Medical Imaging, Lecture Notes in Computer Science, vol. 3565. Springer, Berlin/Heidelberg, pp. 357–376.

Fillard, P., Gerig, G., 2003. Analysis tool for diffusion tensor MR. In: MICCAI'03. LNCS, vol. 2. Springer, pp. 979–980.

Frindel, C., Robini, M., Croisille, P., Zhu, Y.-M., 2009. Comparison of regularization methods for human cardiac diffusion tensor MRI. Medical Image Analysis 13 (3), 405–418.

Gamper, U., Boesiger, P., Kozerke, S., 2007. Diffusion imaging of the in vivo heart using spin echoes – considerations on bulk motion sensitivity. Magnetic Resonance in Medicine 57, 331–337.

Gudbjartsson, H., Patz, S., 2005. The rician distribution of noisy mri data. Magnetic Resonance in Medicine 34 (6), 910–914.

Hansen, P.C., 1992. Analysis of discrete Ill-posed problems by means of the L-curve. SIAM Review 34 (4), 561.

Härdle, W.K., Marron, J.S., 1985. Optimal bandwidth selection in nonparametric regression function estimation. Annals of Statistics 13 (4), 1465–1481.

Hargreaves, B.A., Cunningham, C.H., Nishimura, D.G., Conolly, S.M., 2004. Variable-rate selective excitation for rapid MRI sequences. Magnetic Resonance in Medicine 52, 590–597.

Please cite this article in press as: Toussaint, N., et al. *In vivo* human cardiac fibre architecture estimation using shape-based diffusion tensor processing. Med. Image Anal. (2013), http://dx.doi.org/10.1016/j.media.2013.02.008

Helm, P.A., Tseng, H.J., Younes, L., McVeigh, E.R., Winslow, R.L., 2005. Ex vivo 3D diffusion tensor imaging and quantification of cardiac laminar structure. Magnetic Resonance in Medicine 54 (4), 850–859.

Helm, P.A., Younes, L., Beg, M.F., Ennis, D.B., Leclercq, C., Faris, O.P., McVeigh, E., Kass, D., Miller, M.I., Winslow, R.L., 2006. Evidence of structural remodeling in the dyssynchronous failing heart. Circulation Research 98 (1), 125–132.

Holmes, A.A., Scollan, D., Winslow, R.L., 2000. Direct histological validation of diffusion tensor mri in formaldehyde-fixed myocardium. Magnetic Resonance in Medicine 44 (1), 157–161.

Hsu, E.W., Muzikant, A.L., Matulevicius, S.A., Penland, R.C., Henriquez, C.S., 1998. Magnetic resonance myocardial fiber-orientation mapping with direct histological correlation. American Journal of Physiology – Heart and Circulation Physiology 274, 1627–1634.

Kanai, A., Salama, G., 1995. Optical mapping reveals that repolarization spreads anisotropically and is guided by fiber orientation in guinea pig hearts. Circulation Research 77, 784–802.

Kung, G.L., Nguyen, T.C., Itoh, A., Skare, S., Ingels, N.B., Miller, D.C., Ennis, D.B., 2011. The presence of two local myocardial sheet populations confirmed by diffusion tensor mri and histological validation. Journal of Magnetic Resonance Imaging 34 (5), 1080–1091.

LeGrice, I.J., Takayama, Y., Covell, J.W., 2001. The architecture of the heart: a data-based model. Philosophical Transactions: Mathematical, Physical and Engineering Sciences 359, 1217–1232.

Lombaert, H., Peyrat, J.-M., Croisille, P., Rapacchi, S., Fanton, L., Clarysse, P., Delingette, H., Ayache, N., 2011a. Statistical analysis of the human cardiac fiber architecture from dt-mri. In: Axel, L., Metaxas, D. (Eds.), Proceedings of FIMH Conference 2011, LNCS, vol. 6666. Springer, pp. 171–179, best Paper Award.

Lombaert, H., Peyrat, J.-M., Fanton, L., Cheriet, F., Delingette, H., Ayache, N., Clarysse, P., Magnin, I., Croisille, P., 2011b. Variability of the human cardiac laminar structure. In: Proceedings of STACOM Workshop at MICCAI 2011. Springer.

Mansi, T., Pennec, X., Sermesant, M., Delingette, H., Ayache, N., 2011. iLogDemons: a demons-based registration algorithm for tracking incompressible elastic biological tissues. International Journal of Computer Vision 92 (1), 92–111.

Nielles-Vallespin, S., Mekkaoui, C., Reese, T.G., Gatehouse, P., Feiweier, T., Speier, P., Sosnovik, D.E., Firmin, D., 2011. Fiber tracking of the human heart in vivo. In: Proc. of the Annual Meeting of International Society of Magnetic Resonance in Medicine (ISMRM'11). Abstract 3372.

Nielsen, P.M., Grice, I.J.L., Smaill, B.H., Hunter, P.J., 1991. Mathematical model of geometry and fibrous structure of the heart. American Journal of Physiology – Heart and Circulation Physiology 260, 1365–1378.

Oubel, E., Koob, M., Studholme, C., Dietemann, J.-L., Rousseau, F., 2012. Reconstruction of scattered data in fetal diffusion mri. Medical Image Analysis 16 (1), 28–37.

Peyrat, J.-M., Sermesant, M., Pennec, X., Hervé Delingette, C.X., McVeigh, E.R., Ayache, N., 2006. A computational framework for the statistical analysis of cardiac diffusion tensors: application to a small database of canine hearts. IEEE Transactions in Medical Imaging 25 (5), 612–625.

Powell, M.J.D., 2008. Developments of NEWUOA for minimization without derivatives. Journal of Numerical Analysis, 1–16.

Reese, T.G., Weisskoff, R.M., Smith, R.N., Rosen, B.R., Dinsmore, R.E., Wedeen, V.J., 1995. Imaging myocardial fiber architecture in vivo with magnetic resonance. Magnetic Resonance in Medicine 34, 786–791.

Rohmer, D., Gullberg, G.T., 2006. A Bloch-Torrey Equation for Diffusion in a Deforming Media. Tech. rep., University of California, Technical Report Paper LBNL-61295.

Schär, M., Kozerke, S., Fischer, S.E., Boesiger, P., 2004. Cardiac ssfp imaging at 3 tesla. Magnetic Resonance in Medicine 51 (4), 799–806.

Scollan, D.F., Holmes, A., Zhang, J., Winslow, R.L., 2000. Reconstruction of cardiac ventricular geometry and fiber orientation using magnetic resonance imaging. Annals of Biomedical Engineering 28, 934–944.

Sosnovik, D.E., Wang, R., Dai, G., Reese, T.G., Wedeen, V.J., 2009. Diffusion MR tractography of the heart. Journal of Cardiovascular MR 11, 1–47.

Stejskal, E., Tanner, J., 1965. Spin diffusion measurements: spin echoes in the presence of a time-dependant field gradient. Journal of Chemical Physics 42, 288–292.

Stoeck, C.T., Toussaint, N., Kozerke, S., 2011. Adaptative trigger delay for cardiac diffusion weighted mr. In: Book of Abstracts, International Society in Magnetic Resonance in Medicine, Sockholm, June 2010 (ISMRM'10).

Streeter, D.D., Hanna, W.T., 1973. Engineering mechanics for successive states in canine left ventricular myocardium (II. Fiber angle and sarcomere length). Circulation Research 33, 656–664.

Sutton, M.G.S.J., Sharpe, N., 2000. Left ventricular remodeling after myocardial infarction. Circulation: Cardiovascular Imaging 101, 2981–2988.

Toussaint, N., Mansi, T., Delingette, H., Ayache, N., Sermesant, M., 2008. An integrated platform for dynamic cardiac simulation and image processing: application to personalised tetralogy of fallot simulation. In: Proc. Eurographics Workshop on Visual Computing for Biomedicine (VCBM). Delft, The Netherlands.

Toussaint, N., Sermesant, M., Fillard, P., 2007. vtkinria3d: a vtk extension for spatiotemporal data synchronization, visualization and management. In: Proc. of Workshop on Open Source and Open Data for MICCAI. Brisbane, Australia.

Toussaint, N., Stoeck, C.T., Kozerke, S., Sermesant, M., Batchelor, P.G., September 2010. In vivo human 3D cardiac fibre architecture: reconstruction using curvilinear interpolation of diffusion tensor images. In: Proc. Medical Image Computing and Computer Assisted Intervention (MICCAI'10). Lecture Notes in Computer Science. Beijing, China.

Tseng, W.-Y.I., Reese, T.G., Weisskoff, R.M., Wedeen, V.J., 1999. Cardiac diffusion tensor MRI in vivo without strain correction. Magnetic Resonance in Medicine 42, 393–403.

Weinstein, D., Kindlmann, G., Lundberg, E., 1999. Tensorlines: advection–diffusion based propagation through diffusion tensor fields. In: Proceedings of the Conference on Visualization '99: Celebrating Ten Years. VIS '99. IEEE Computer Society Press, Los Alamitos, CA, USA, pp. 29–253.

Wu, M.-T., Su, M.-Y.M., Huang, Y.-L., Chiou, K.-R., Yang, P., Pan, H.-B., Reese, T.G., Wedeen, V.J., Tseng, W.-Y.I., 2009. Sequential changes of myocardial microstructure in patients postmyocardial infarction by diffusion-tensor cardiac MR. Circulation: Cardiovascular Imaging 2, 32–40.

Yang, F., Zhu, Y.-M., Magnin, I.E., Luo, J.-H., Croisille, P., Kingsley, P.B., 2012. Feature-based interpolation of diffusion tensor fields and application to human cardiac dt-mri. Medical Image Analysis 16 (2), 459–481.

Please cite this article in press as: Toussaint, N., et al. *In vivo* human cardiac fibre architecture estimation using shape-based diffusion tensor processing. Med. Image Anal. (2013), http://dx.doi.org/10.1016/j.media.2013.02.008